Appendices

1. Geological background and samples

The Hamersley Basin in Western Australia contains the world's most extensive BIFs (1). The late Neoarchean to early Paleoproterozoic Hamersley Group includes three major BIF units that are "Superior-type" (deposited on broad continental shelves in a passive margin), which are, from older to younger, the Marra Mamba, Brockman, and Boolgeeda iron formations. The Dales Gorge member of the lowermost part of the Brockman Iron Formation (IF) is the subject of this study (Figure S1). The depositional age of the Dales Gorge member lies between 2.50 Ga and 2.45 Ga (2). The Dales Gorge member is approximately 160-140 m thick, consisting of 17 iron-rich, m-scale macrobands and 16 shale macrobands, named BIF0-BIF16 and S1-S16, respectively (Figure S1). The m-scale iron-rich macrobands are each composed of cm-scale iron-rich mesobands, which in turn contain numerous sub-mm microbands (3). Metamorphic grade is estimated at lower greenschist facies (4).

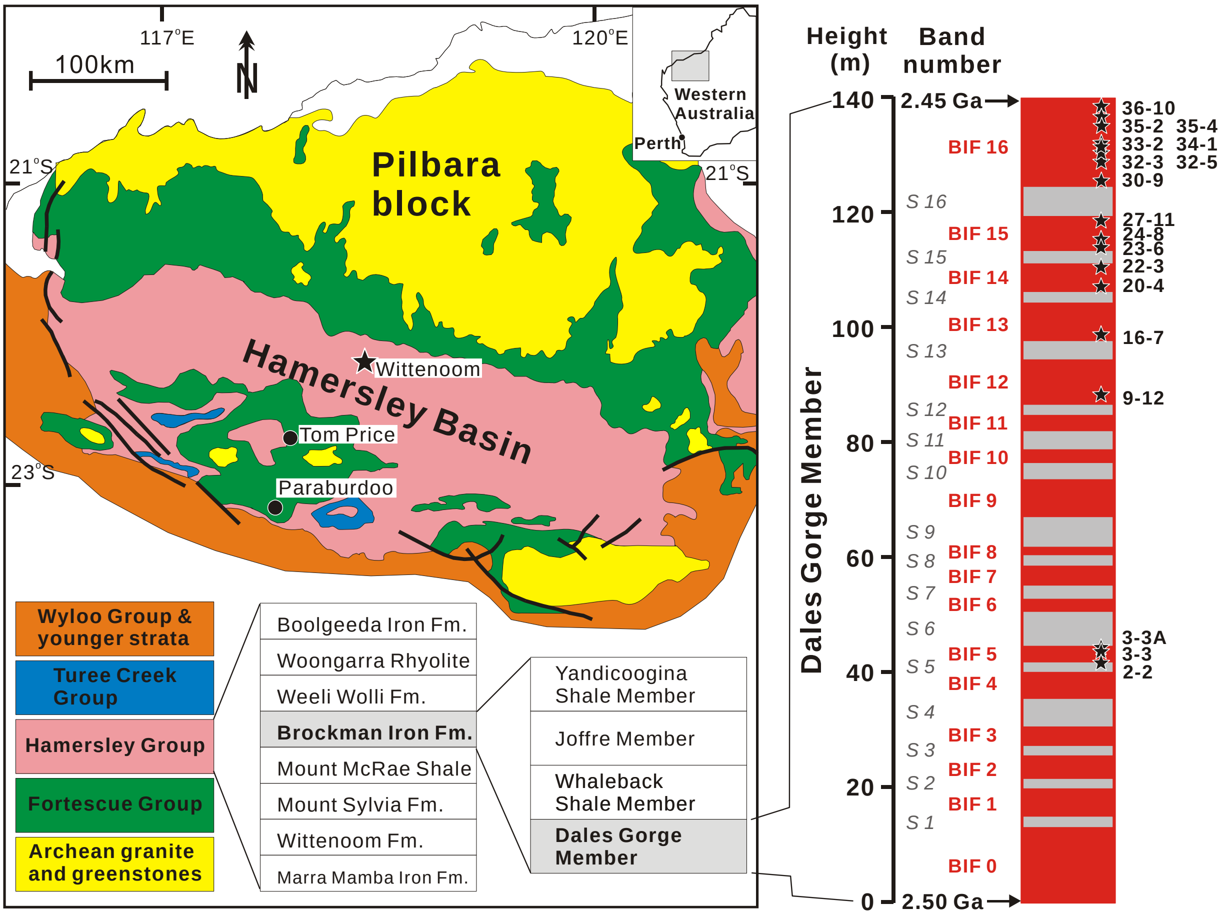

Figure S1. Geologic map of the Hamersley Basin and stratigraphic section of the Dales Gorge member BIF of the Brockman Iron Formation. Figure modified after ref. (5). The 2.50-2.45 Ga age for the Dales Gorge member BIF was based on zircon U-Pb geochronology (2).

The BIF samples analyzed in this study come from diamond drill core DDH-47A that was drilled ~15 km south of Wittenoom, Western Australia (star in Figure S1). DDH-47A is the type section core for the Dales Gorge member that has been described in detail (3). This drill core has been studied in previous C, O, and Fe isotope investigations using mg-sized, bulk-sampling techniques (6-8), and *in situ* O, Si, and Fe isotope analyses by Heck et al. (9) and Li et al. (5). More details of the DDH-47A drill core, including original photos of the complete drill core set, are provided in Huberty et al. (10).

Magnetite and hematite are the typical Fe-bearing minerals in the DDH-47A drill core samples (Figure S2). Based on reflected-light microscopy and detailed BSE imaging, Huberty et al. (10) and Li et al. (5) divided the iron oxide mineralogy of the BIF samples into three groups. The first group is *euhedral magnetite,* which occurs as discrete, large (typically >50 µm), euhedral, apparently-homogeneous grains that are interpreted as a recrystallization texture. Euhedral magnetite commonly occurs in samples that contain predominantly hematite but minor magnetite (e.g., Figure S2). The other two groups of magnetite are termed *silician magnetite* and *low-Si magnetite*, where the former contains 1-3 wt. % SiO_2 in the magnetite structure and the latter contains <1 wt. % SiO_2. The silician and low-Si magnetite have distinctive contrast in BSE images, and silician magnetite commonly forms overgrowths to low-Si magnetite domains (Figure S2; ref. 9). Silician magnetite and low-Si magnetite commonly occur in BIF samples that contain extensive magnetite layers but no hematite. *In situ* O isotope analyses using SIMS show that hematite has the lowest $\delta^{18}O_{SMOW}$ values (mostly between -8 and -4 ‰), low-Si magnetite has higher $\delta^{18}O_{SMOW}$ values and a wide $\delta^{18}O_{SMOW}$ range (-7 to +3 ‰), and silician magnetite and euhedral magnetite have the highest $\delta^{18}O_{SMOW}$ values (+2 to +6 ‰). Samples that have lower $\delta^{18}O_{SMOW}$ values are interpreted to be less affected by burial metamorphism, whereas the higher $\delta^{18}O_{SMOW}$ values reflect re-equilibration at elevated temperatures, reflecting compositions that are furthest from near-primary conditions (5).

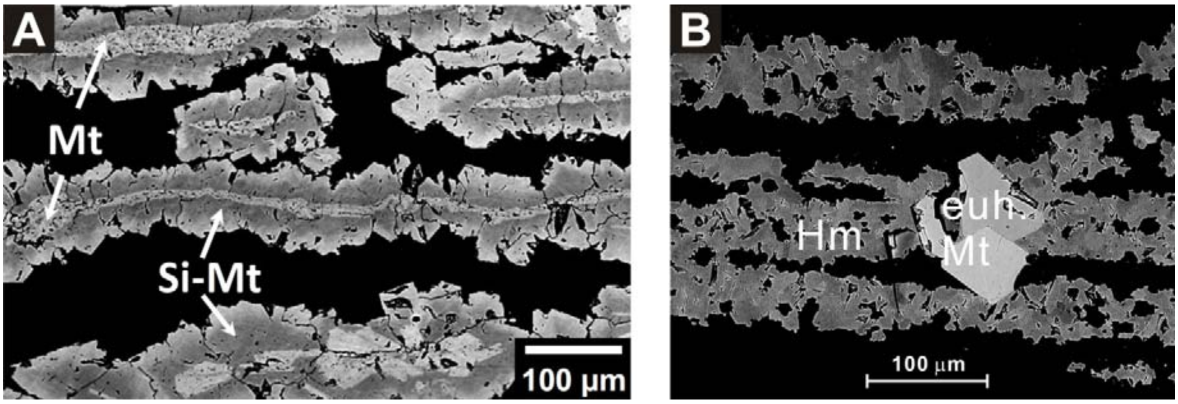

Figure S2. Representative Fe-oxide mineral textures. Mt: low Si magnetite, Si-Mt: Silician magnetite, euh. Mt: euhedral magnetite, Hm: hematite.

2. Analytical methods

2.1 Sample preparation

Centimeter- or sub-centimeter sized samples were cut from the drill core and were embedded into 1-inch round epoxy plugs. For *in situ* Fe isotope and REE analyses, the plugs were polished using a protocol described in Heck et al. (9). Small chips (typically 200-500 mg) were cut from drill core, and subsequently cleaned using acetone, 0.2 M HCl, and 18.2 MΩ H_2O in an ultrasonic bath for more than 10 min to remove surface contamination. The chips were dried and weighed before bulk-rock isotope and elemental analyses.

Rock chips (~300 mg) were digested using a mixture of 2 ml double-distilled 29 M HF, 1 ml double-distilled 8 M HCl, and 1ml 14 M Optima® grade HNO_3 in capped Savillex beakers that were heated overnight at 130 °C. A mixed REE spike (^{142}Ce, ^{150}Nd, ^{149}Sm, ^{151}Eu, ^{155}Gd, ^{161}Dy, ^{167}Er, ^{171}Yb) was added to each sample to measure elemental concentrations by isotope dilution mass spectrometry (IDMS). HF was used to dissolve any quartz that may have been present, and HCl was used to stabilize Fe^{3+} and suppress formation of iron fluoride. After overnight digestion, the samples were dried and the digestion procedure was repeated. The samples were then converted to chloride form using double-distilled 8 M HCl. The solutions were checked under a binocular microscope to ensure that the entire sample had dissolved and that no fluorides were present.

After complete digestion, the samples were dissolved in 2ml 2.5 M HCl, and this solution (*stock sample solution*) was used for subsequent bulk-rock elemental and isotopic analysis.

2.2 Bulk sample REE, Nd, and Fe isotope analysis

A 1.6 ml aliquot of the *stock sample solution* was taken for Nd isotope analysis and REE concentration analysis by IDMS. REEs were separated from major elements using cation-exchange resin and 2.5M HCl, followed by collection of a bulk REE cut using 6M HCl. Separation of the REEs was performed using 2-methylactic acid and cation-exchange resin in NH_4^+ form and REE cuts were sequentially collected that contained the heavy REE (Yb, Er, Dy), the middle REE (Gd, Eu, Sm), a Nd cut, and a Ce cut. Total Nd procedural blanks were ≤70 pg, which was less than 0.003 % of the amount of Nd in the lowest Nd concentration sample; no blank corrections were applied. Neodymium isotope compositions were measured using a VG Instruments *Sector 54* thermal ionization mass spectrometer, analyzed as NdO^+ using a dynamic multi-collection analysis routine. Samples were loaded onto Re filaments with Si-gel and H_3PO_4 and an O_2 gas bleed was set to a pressure in the source of 5×10^{-7} mbar. Instrumental mass fractionation was corrected using an exponential law relative to ^{146}Nd/^{144}Nd=0.7219. Reported isotope ratios are the average of 150 ratios. Typical mass 160 (^{144}Nd^{16}O^{+}) ion signals were 5×10^{-12} amps. The measured ^{143}Nd/^{144}Nd for the La Jolla Nd standard was 0.511850±0.000009 (2-SD; n=10) and internal laboratory standards AMES I and II yielded ^{143}Nd/^{143}Nd ratios of 0.512147±0.000018 (2-SD; n=6) and 0.511966±0.000004 (2-SD; n=6), respectively.

Because the REEs were measured on the exact same aliquot used for Fe and Nd isotope analysis, REEs were determined by IDMS; such an approach does not allow for analysis of non-mono-isotopic REEs or Y. For the IDMS analyses the different REE cuts were analyzed using a Micromass *IsoProbe* with mass-bias correction based on sample-standard bracketing. An *Aridus* desolvating nebulizer was used with a *Savillex* 50µl/min concentric flow nebulizer. For the HREEs, IDMS was based on simultaneous analysis of ^{161}Dy/^{163}Dy, ^{167}Er/^{166}Er, and ^{171}Yb/^{174}Yb. Samples were diluted to a concentration of approximately 30, 25, and 10 ppb for Dy, Er, and Yb, respectively, and standard solutions that bracketed the range of sample concentrations were analyzed to correct for mass bias. For the MREEs, IDMS was based on simultaneous analysis of ^{149}Sm/^{147}Sm, ^{151}Eu/^{153}Eu and ^{155}Gd/^{158}Gd, with mass 156 monitored to evaluate any Dy isobars, which were found to be negligible. Samples were diluted to a concentration of approximately 40, 15, and 15 ppb for Sm, Eu, and Gd, respectively, with standards that bracketed the range in concentrations of samples used for mass-bias correction. Cerium IDMS was based on analysis of ^{142}Ce/^{140}Ce with monitoring of mass 146 to evaluate for Nd isobars, which were found to be negligible. Samples were diluted to approximately 30ppb and standards were run that bracketed the range in Ce sample concentrations. Based on analysis of variable concentration REE standards that were run as samples, isotope ratios for Ce, Sm, Eu, Gd, Dy, Er, and Yb are precise to ±0.1%.

A 5 µl aliquot of the *stock sample solution* was taken for Fe isotope analysis. Iron was purified using an established anion-exchange procedure (11-12). Iron solutions were diluted to 600 ppb and isotopic measurements were conducted using a Micromass *IsoProbe* MC-ICP-MS and an *Aridus* desolvating nebulizer aspirating at ~50 µl/min. Mass spectrometry followed the procedures reported by Beard et al.

(11). Isotopic data are reported as $^{56}Fe/^{54}Fe$ and $^{57}Fe/^{54}Fe$ ratios in standard delta (δ) notation, in units of per mil (‰), and using the average of igneous rocks as the standard reference reservoir (11):

$$\delta^{56}Fe = [(^{56}Fe/^{54}Fe)_{sample}/(^{56}Fe/^{54}Fe)_{standard}-1] \times 1000$$

Relative to the average of igneous rocks, the international Fe isotope standard IRMM-014 has a $\delta^{56}Fe$ value of -0.09‰ on this scale (11). The external long-term reproducibility (2-SD) for $\delta^{56}Fe$ measurements using this method is ±0.08‰, as determined from analysis of multiple in-house Fe standard solutions, and synthetic samples (Fe standard solutions doped with matrix elements) that were processed through the ion-exchange procedure together with drill core samples.

2.3 Bulk sample Al and Fe content analysis

A 5 µl aliquot of each *stock sample solution* was taken for bulk-sample Al and Fe concentration measurements to assess the potential for siliciclastic components in the sampled iron-rich bands. Each aliquot was diluted volumetrically by 2×10^3-10^4 times using double-distilled water, to make a solution that contains approximately 5-50 ppm Fe. The concentration of Fe in the diluted solution was measured using the *Ferrozine*® method (13). Gravimetrically prepared Fe standard solutions that contained 1, 5, 10, 25, 50, and 100 ppm Fe were used as the calibration standards. Iron contents of the BIF samples were calculated from the measured Fe content, dilution factor, and original weight of the samples.

An aliquot of the *diluted stock sample solution* that was used for Fe content measurements was further diluted by a factor of ten, and was analyzed using a Nu Instruments *Nu Plasma II* MC-ICP-MS for Al contents. A set of gravimetrically prepared Fe-Al mixed solutions were used as the calibration standards. Matrix effects of Fe and other elements was assessed by analysis of Fe-Al mixed solutions that had different elemental ratios, and matrix issues were found to be negligible on measured intensity of Al on the *Nu Plasma II* MC-ICP-MS. The Al contents of the BIF samples were calculated from the measured Al content, dilution factor, and original weight of samples. The results of these analyses are reported as Al_2O_3 and Fe_2O_3 (as total Fe) in Table S1.

2.4 *In situ* Fe isotope analysis

In situ Fe isotope analysis was performed to determine fine-scale temporal variations in Fe isotope compositions in the BIF samples studied using "bulk" techniques. Isotopic analysis was done using a femtosecond Laser Ablation (fs-LA) MC-ICP-MS system that consists of a femtosecond source laser that produces an output 266 nm beam, a Photon-Machines beam-delivery system, a Photon-Machines *HelEX* ablation cell, and a Micromass *IsoProbe* MC-ICP-MS. Laser ablation analysis was made using a spot size of 11µm in raster mode, a stage translation speed of 1 µm/s, and an ablation area that was typically a rectangle area of 40×40 µm. For samples that had elongated shapes, analysis consisted of non-rectangular rasters at 1 µm/s. Details of the operating conditions of the fs-LA system can be found in Li et al. (5), and d'Abzac (14).

A standard-sample-standard bracketing method was used for mass-bias and instrument drift correction. A magnetite in-house standard and a hematite in-house standard were used as the matrix-matching standards for fs-LA Fe isotope analysis. Using matrix-matching standards and the *HelEX* cell, total Fe ion intensities of standards and samples were typically matched within 5 %, except for analyses in which quartz was accidentally ablated. The internal precision of each Fe isotope analysis was typically better than 0.12 ‰ (2 SE) in both $\delta^{56}Fe$ and $\delta^{57}Fe$ values. Measured $\delta^{56}Fe$ and $\delta^{57}Fe$ values followed a mass-dependent relation (5). External precision (reproducibility) of the fs-LA analysis was better than ±0.2 ‰ (2SD) in $\delta^{56}Fe$, based on repeat analyses of the same magnetite and hematite standards within an analytical session and over multiple sessions. Accuracy of fs-LA MC-ICP-MS Fe isotope analysis lies within the limits of external reproducibility (<0.2 ‰ in $\delta^{56}Fe$, 2 SD; ref. 5).

2.5 *In situ* REE analysis

In situ REE analysis was performed to determine the magnetite generation that contained the major repository of REEs to evaluate the relative influence of near-primary oxides and metamorphic/ hydrothermal magnetite on the "bulk" Nd isotope analyses. To our knowledge, this is the first time the Nd mass balance was determined on a micron scale for BIF samples analyzed for Nd isotopes, but is critical to address which generation of oxides controls the Nd isotope composition of the sample. REE analysis was done using a system that consists of a Photon-Machines femtosecond laser and a *Nu Plasma II* MC-ICP-MS with multiple ion counting on mass numbers 141(Pr), 143(Nd), 145(Nd), 146(Nd), and 147(Sm). Laser-ablation analysis was made using a spot size of 11µm in raster mode, typically adjacent to the laser ablation pits of *in situ* Fe isotope analysis or *in situ* O isotope analysis (5). Glass standards of BHVO, SRM-612, BCR-2, and GSD-1 were analyzed under the same instrumental conditions before and after the analytical session to determine ion intensity calibration and instrumental drift. Each *in situ* REE analysis consisted of a 60s on-peak gas blank measurement, followed by 40×1s integrations with the laser firing. For the range of samples measured, the ^{147}Sm count rate was 28±19 cps for low-Si magnetite, 9±8 cps for silician magnetite, 7±12 cps for euhedral magnetite, and 22±18 cps for hematite; the ^{146}Nd and ^{141}Pr count rates were 106±73 and 159±111 for low-Si magnetite, 26±22 and 36±22 for silician magnetite, 26±46 and 35±59 for euhedral magnetite, and 77±59 and 107±81 for hematite, respectively. Based on these average count rates, and assuming precision is equal to the square root of the number of counts, the precision for Sm, Nd, and Pr are estimated to be 4, 2, and 1.5%, respectively.

3. Elemental and isotopic compositions

3.1 Bulk sample Al, Fe, Nd, and REE data

Table S1. Nd and Fe isotope composition and Fe-Al-REE content of BIF chip samples by bulk dissolution.

Lab ID	Vertical position (m)	Macro -band No.	Sample ID	Ce (ppm)	Nd (ppm)	Sm (ppm)	Eu (ppm)	Gd (ppm)	Dy (ppm)	Er (ppm)	Yb (ppm)	Eu* (PAAS norm.)	Sm/Nd (PAAS norm.)	^{147}Sm/^{144}Nd	^{143}Nd/^{144}Nd	eNd (2.5Ga)	δ^{56}Fe (‰)	Fe_2O_3 (wt%)	Al_2O_3 (wt%)
3N-453	42	DB-5	2-2	5.890	3.062	0.783	0.297	0.991	0.942	0.599	0.603	1.55	1.56	0.1543	0.511877	-1.20	-0.25		
3N-454	43	DB-5	3-3	34.221	15.135	3.263	1.640	5.269	5.814	4.259	3.608	1.77	1.32	0.1301	0.511481	-1.17	-0.22		
3N-455	43	DB-5	3-3A	12.733	7.113	1.956	1.064	2.771	2.640	1.607	1.538	2.08	1.68	0.1659	0.512019	-2.19	-0.83	21.8	0.37
3N-456	87	DB-12	9-12	2.069	0.931	0.190	0.075	0.228	0.224	0.165	0.231	1.68	1.24	0.1230	0.511519	1.90	0.09	32.9	0.09
3N-457	98	DB-13	16-7	7.537	3.713	0.717	0.299	1.243	1.324	1.034	0.952	1.40	1.18	0.1165	0.511258	-1.15	0.35	36.5	0.11
3N-459	106	DB-14	20-4	1.219	0.494	0.095	0.044	0.158	0.188	0.153	0.181	1.61	1.18	0.1166	0.511362	0.86	1.30	18.1	0.07
3N-460	109	DB-14	22-3	0.248	0.109	0.025	0.011	0.043	0.069	0.093	0.142	1.43	1.42	0.1399	0.511602	-1.96	-0.13		
3N-461	112	DB-15	23-6	11.334	3.714	0.497	0.154	0.469	0.310	0.170	0.141	1.50	0.82	0.0808	0.510881	3.01	0.33		
3N-462	115	DB-15	24-8	2.735	1.053	0.156	0.055	0.178	0.144	0.109	0.116	1.54	0.90	0.0892	0.510970	2.03	0.11	36.7	0.22
3N-463	119	DB-15	27-11	5.979	1.777	0.270	0.083	0.228	0.179	0.143	0.252	1.57	0.93	0.0915	0.510968	1.25	0.11	28.1	1.41
3N-464	126	DB-16	30-9	6.192	2.638	0.570	0.184	0.532	0.454	0.306	0.397	1.57	1.32	0.1304	0.511536	-0.17	-0.13	41.4	0.61
3N-465	130.6	DB-16	32-3	1.166	0.617	0.139	0.063	0.248	0.281	0.244	0.213	1.48	1.37	0.1355	0.511576	-1.06	-0.48		
3N-466	130.2	DB-16	32-5	0.530	0.216	0.041	0.017	0.054	0.056	0.047	0.089	1.67	1.16	0.1150	0.511314	0.44	-0.22	20.0	0.13
3N-467	132.6	DB-16	33-2	3.126	1.413	0.308	0.116	0.401	0.400	0.277	0.260	1.51	1.33	0.1316	0.511596	0.63	0.21	19.6	0.11
3N-468	134.5	DB-16	34-1	1.257	0.604	0.127	0.062	0.192	0.186	0.149	0.164	1.79	1.29	0.1271	0.511498	0.15	0.31	22.5	0.06
3N-469	136	DB-16	35-2	0.995	0.509	0.121	0.061	0.218	0.279	0.253	0.221	1.64	1.45	0.1437	0.511705	-1.18	-0.66	28.5	0.03
3N-470	135.6	DB-16	35-4	1.282	0.670	0.138	0.060	0.226	0.230	0.154	0.144	1.52	1.26	0.1243	0.511411	-0.65	0.10		
3N-471	136.6	DB-16	36-10	0.503	0.200	0.042	0.020	0.080	0.114	0.120	0.127	1.53	1.29	0.1274	0.511481	-0.28	-0.48	7.1	0.08

3.2 *In situ* Fe data

3.2.1 Test of lateral Fe isotope variability in BIF samples

Stable Fe isotope analysis of individual BIF microbands (<1 mm thick) was used to investigate potential variations in Fe sources (continental versus hydrothermal) on the smallest scale of BIF banding that have been proposed to record annual records (15-16). A key question is possible lateral heterogeneity and inter-microband heterogeneity. The possibility of mm-scale lateral Fe isotope heterogeneity was investigated using a representative BIF sample (Figure S3). Based on counting of the number of microbands, and the assumption that each microband represents an annual varve-like feature (15-17), the 5-mm-thick sample records a period of about 80-100 years (80-100 magnetite layers). A compacted sediment depositional rate of 50-63 m/Ma is estimated based on this sample. This rate is consistent with the rate estimated by Trendall et al. (2) for the Dales Gorge member BIF based on zircon U-Pb geochronology, which is 5-180 m/Ma for compacted sediment. Trendall et al. (2) noted that the main uncertainty in the estimation of depositional rates is the uncertainty in the time required for deposition of the shale macro bands in the Dales Gorge member. High density *in situ* Fe isotope analysis was performed along and across the magnetite microbands (Figure S3). The measured δ^{56}Fe values cluster around -0.6‰, with limited scatter within ±0.2 ‰, the 2SD external precision of the *in situ* laser ablation method.

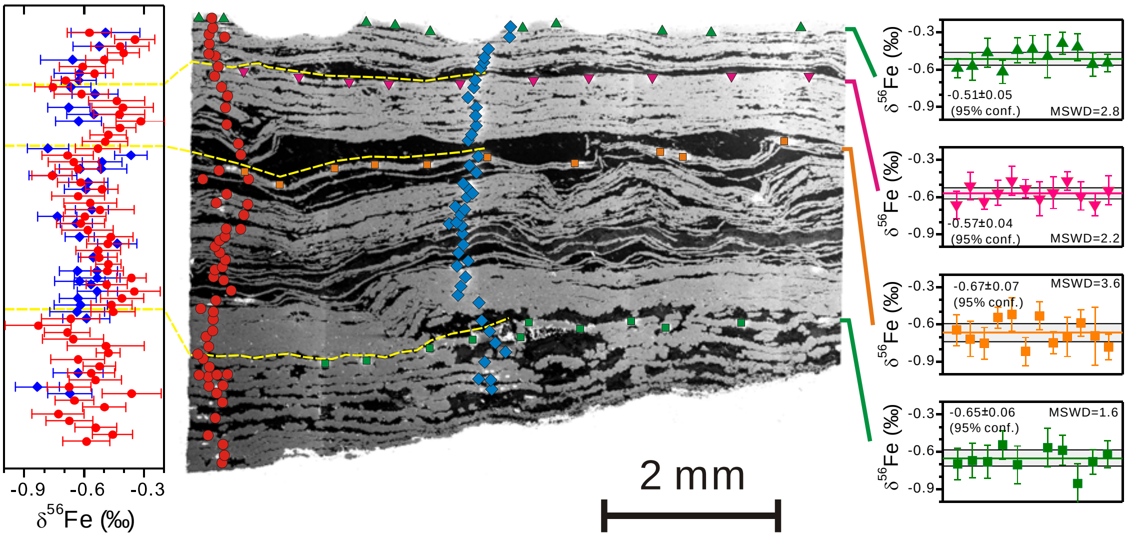

Figure S3. Map of high density *in situ* Fe isotope analysis of typical magnetite microbands in BIF sample 3-3A. The center figure is a BSE image of the BIF drill core chip, where magnetite layers are light colored, and quartz and silicates are black or dark gray. Error bars in isotope plots represent 2SE internal uncertainty. Red circles and blue diamonds denote laser ablation analyses made in two different analytical sessions in an attempt to assess Fe isotope variability between layers. Colored triangles and squares denote laser ablation analyses made in another analytical session in an attempt to assess Fe isotope homogeneity within single layers. The details of spatial context of each laser point, and the corresponding Fe isotope data, are provided in Figure S4, and Table S2, respectively. Weighted average and associated error (95% confidence), together with MSWD values, are calculated using *Isoplot*®. It should be noted that the MSWD values are all slightly greater than 1, which implies that the internal error for single Fe isotope measurements might be slightly underestimated.

Figure S4. Details of magnetite microband texture and analysis number for vertical and horizontal transects of in situ Fe isotope analyses on sample 3-3A in BIF band 5. Magnetite layers and grains are in gray, and quartz is in black.

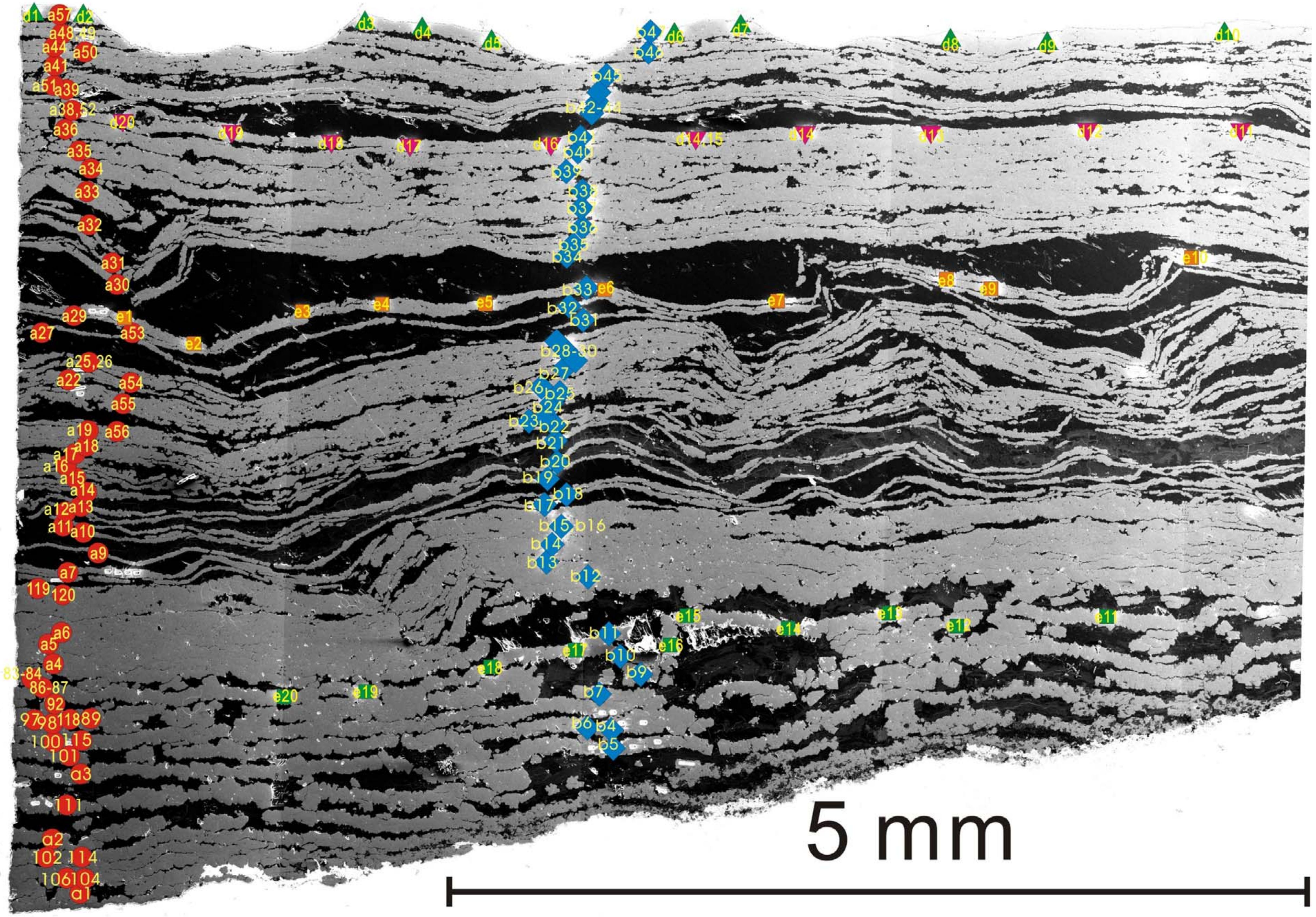

Table S2. Iron isotope data for test of Fe isotope heterogeneity in sample 3-3A-d in BIF band 5, which was shown in Figure S3. Analysis number for each individual in situ analysis is shown in Figure S4.

Analysis No.	**Fe intensity relative to standard**	**δ^{56}Fe**	**2se**	**$\delta^{57/54}$Fe**	**2se**
Left vertical transect (marked with red circle) in Fig. A3 and Fig. A4					
a1	0.98	-0.59	0.12	-0.85	0.07
106	1.00	-0.46	0.10	-0.69	0.06
104	1.03	-0.54	0.10	-0.69	0.08
114	1.02	-0.67	0.12	-0.90	0.08
102	1.03	-0.73	0.13	-1.06	0.08
a2	0.98	-0.50	0.11	-0.75	0.07
111	1.02	-0.65	0.10	-0.79	0.05
101	1.03	-0.68	0.11	-0.99	0.07
100	1.03	-0.54	0.13	-0.71	0.07
97-98	0.96	-0.56	0.12	-0.70	0.08
88	1.00	-0.52	0.08	-0.86	0.05
89	1.02	-0.63	0.13	-0.79	0.07
118	1.03	-0.48	0.06	-0.85	0.05
92	1.02	-0.49	0.19	-0.67	0.13
87	0.99	-0.66	0.15	-1.01	0.08
86	0.99	-0.69	0.11	-0.88	0.06
83-84	0.96	-0.67	0.14	-0.83	0.08
a4	0.96	-0.45	0.11	-0.67	0.07
a5	0.97	-0.46	0.10	-0.71	0.08
a6	0.97	-0.41	0.11	-0.52	0.08
119	0.96	-0.35	0.13	-0.44	0.09
120	0.93	-0.49	0.10	-0.55	0.09
a7	0.99	-0.36	0.07	-0.62	0.06
a9	1.00	-0.48	0.08	-0.75	0.04
a10	0.98	-0.48	0.06	-0.66	0.04
a11	0.97	-0.53	0.09	-0.84	0.06
a12	0.98	-0.53	0.11	-0.65	0.05
a13	0.95	-0.48	0.11	-0.68	0.06
a14	0.96	-0.47	0.11	-0.76	0.09
a15	0.97	-0.58	0.13	-0.81	0.06
a16	0.96	-0.62	0.12	-0.77	0.05
a17	0.97	-0.60	0.11	-0.82	0.06
a18	0.92	-0.52	0.17	-0.62	0.09
a19	0.97	-0.57	0.13	-0.70	0.07
a25	0.99	-0.76	0.10	-1.07	0.07
a26	1.00	-0.63	0.11	-1.02	0.10
a27	1.00	-0.65	0.13	-0.80	0.07
a29	0.99	-0.53	0.11	-0.83	0.07
a30	0.98	-0.49	0.11	-0.83	0.08
a31	1.01	-0.48	0.09	-0.80	0.07
a32	0.99	-0.42	0.08	-0.74	0.06
a33	0.96	-0.32	0.12	-0.60	0.11
a34	0.99	-0.42	0.13	-0.52	0.07
a35	0.97	-0.41	0.15	-0.60	0.07

Analysis No.	Fe intensity relative to standard	δ^{56}Fe	2se	$\delta^{57/54}$Fe	2se
a36	0.97	-0.44	0.14	-0.63	0.07
a38	0.99	-0.76	0.09	-0.97	0.05
a39	1.01	-0.69	0.07	-0.90	0.08
a41	0.98	-0.61	0.12	-1.01	0.07
a44	0.97	-0.40	0.08	-0.59	0.05
a48	0.96	-0.35	0.10	-0.69	0.06
a49	0.97	-0.42	0.15	-0.70	0.07
a50	0.99	-0.50	0.09	-0.78	0.06
a51	0.98	-0.55	0.10	-0.80	0.06
a52	0.99	-0.61	0.14	-0.94	0.05
a53	0.98	-0.68	0.13	-0.91	0.09
a54	0.98	-0.62	0.12	-0.92	0.06
a55	0.97	-0.51	0.08	-0.78	0.07
a56	0.95	-0.63	0.13	-0.95	0.10
a57	0.95	-0.57	0.11	-0.70	0.08
Right vertical transect (marked with blue diamond) in Fig. A3 and Fig. A4					
b5	1.00	-0.87	0.12	-1.12	0.09
b6	0.99	-0.83	0.11	-1.36	0.08
b7	0.97	-0.63	0.12	-0.99	0.07
b10	0.94	-0.59	0.12	-0.97	0.07
b11	0.99	-0.63	0.14	-0.83	0.07
b12	1.02	-0.62	0.13	-0.79	0.10
b13	1.00	-0.63	0.09	-0.93	0.08
b14	0.97	-0.53	0.10	-0.93	0.07
b15	1.01	-0.56	0.09	-0.94	0.06
b16	1.02	-0.62	0.13	-0.86	0.08
b18	0.99	-0.53	0.12	-0.98	0.07
b19	0.98	-0.54	0.10	-0.74	0.08
b20	0.99	-0.55	0.07	-0.87	0.06
b21	1.00	-0.43	0.10	-0.79	0.07
b22	1.02	-0.62	0.07	-0.74	0.06
b23	0.98	-0.64	0.08	-0.88	0.06
b24	0.97	-0.73	0.10	-1.02	0.07
b25	0.98	-0.56	0.08	-0.78	0.05
b26	0.99	-0.63	0.09	-0.97	0.06
b27	1.03	-0.59	0.11	-0.89	0.08
b28	1.00	-0.58	0.10	-0.76	0.06
b29	0.97	-0.76	0.12	-0.98	0.09
b30	1.00	-0.62	0.10	-0.83	0.05
b31	0.97	-0.51	0.10	-0.95	0.07
b32	1.00	-0.36	0.08	-0.71	0.06
b33	0.96	-0.78	0.10	-1.04	0.06
b37	1.00	-0.63	0.12	-0.97	0.07
a29'	0.97	-0.51	0.15	-0.80	0.07
b38	0.99	-0.55	0.14	-0.71	0.09
b39	0.99	-0.68	0.11	-0.85	0.08
b40	0.97	-0.51	0.13	-0.91	0.10

Analysis No.	**Fe intensity relative to standard**	**δ^{56}Fe**	**2se**	**$\delta^{57/54}$Fe**	**2se**
b41	0.98	-0.55	0.12	-0.94	0.08
b42	0.97	-0.67	0.10	-1.03	0.05
b43	0.97	-0.63	0.09	-0.95	0.09
b44	0.99	-0.62	0.13	-0.88	0.06
b45	0.98	-0.66	0.16	-1.04	0.12
a44'	0.97	-0.51	0.10	-0.87	0.05
b46	0.96	-0.52	0.13	-0.95	0.09
b47	0.99	-0.49	0.17	-0.91	0.11
b48	0.99	-0.67	0.11	-1.02	0.06
1st horizontal transect (marked with green triangle) in Fig. A3 and Fig. A4					
d1	0.96	-0.59	0.07	-0.70	0.04
d2	0.98	-0.46	0.12	-0.75	0.09
d3	1.00	-0.62	0.09	-0.78	0.07
d4	0.98	-0.45	0.10	-0.80	0.07
d5	1.00	-0.44	0.11	-0.73	0.07
d6	1.01	-0.39	0.09	-0.75	0.04
d7	1.00	-0.42	0.11	-0.78	0.06
d8	0.98	-0.56	0.10	-0.69	0.06
d9	0.99	-0.55	0.07	-0.75	0.05
2nd horizontal transect (marked with purple triangle) in Fig. A3 and Fig. A4					
d11	1.01	-0.66	0.11	-0.80	0.06
d12	0.99	-0.51	0.11	-0.77	0.05
d13	1.00	-0.63	0.06	-0.88	0.05
d14	0.99	-0.57	0.10	-0.85	0.06
d15	0.99	-0.47	0.12	-0.82	0.08
d16	1.00	-0.53	0.07	-0.78	0.07
d17	0.99	-0.56	0.13	-0.82	0.06
d18	1.00	-0.47	0.07	-0.83	0.07
d19	1.00	-0.59	0.11	-0.79	0.06
d20	0.97	-0.66	0.09	-0.89	0.07
3rd horizontal transect (marked with brown rectangle) in Fig. A3 and Fig. A4					
e1	0.97	-0.65	0.13	-0.93	0.07
e2	0.98	-0.72	0.14	-1.07	0.09
e3	0.99	-0.75	0.13	-0.96	0.08
e4	0.98	-0.54	0.08	-0.86	0.07
e5	0.98	-0.52	0.13	-0.95	0.08
e6	0.98	-0.82	0.11	-1.13	0.08
e7	0.99	-0.75	0.09	-1.06	0.05
e8	0.94	-0.70	0.16	-1.00	0.12
e9	0.99	-0.59	0.11	-0.88	0.06
e10	0.88	-0.69	0.23	-0.95	0.12
4th horizontal transect (marked with green rectangle) in Fig. A3 and Fig. A4					
e11	0.97	-0.70	0.12	-0.98	0.08
e12	0.97	-0.67	0.14	-0.93	0.08
e13	0.97	-0.68	0.13	-0.97	0.07
e14	0.99	-0.55	0.11	-0.91	0.08
e15	0.98	-0.70	0.15	-1.05	0.08

Analysis No.	Fe intensity relative to standard	δ^{56}Fe	2se	$\delta^{57/54}$Fe	2se
e16	0.98	-0.57	0.15	-0.92	0.07
e18	0.95	-0.85	0.16	-1.13	0.07
e19	0.97	-0.68	0.10	-0.89	0.05
e20	0.96	-0.62	0.11	-0.94	0.08

3.2.2 Fe isotope data of the 7cm-long drill core in Figure 3 of the paper

For *in situ* Fe isotope analysis, the 7cm long drill core was evenly cut into 5 pieces, each piece was embedded into a 2.5-cm round epoxy plug, with in-house hematite and magnetite standards surrounding the sample. The results are shown in Figure 3 and Table S3.

Table S3. Iron isotope data of sample 36-10 in BIF band 16, which was shown in Figure 3. Analysis number for each individual *in situ* analysis is shown in Figure S4.

Position along drill core (mm)	Analysis number	Fe intensity relative to standard	δ^{56}Fe	2SE	δ^{57}Fe	2SE
Magnetite						
1.4	36-10a_mt1	0.96	-0.75	0.10	-1.11	0.07
2.9	36-10a_mt2	0.95	-0.85	0.07	-1.10	0.07
4.3	36-10a_mt3	0.96	-0.90	0.07	-1.24	0.07
5.7	36-10a_mt4	0.87	-0.77	0.23	-1.18	0.13
7.1	36-10a_mt5	0.94	-0.63	0.09	-0.99	0.07
8.6	36-10a_mt6	0.91	-0.76	0.10	-1.07	0.09
8.6	36-10a_mt6a	0.95	-0.73	0.10	-1.19	0.07
10	36-10a_mt7	0.95	-0.70	0.08	-0.97	0.04
11.4	36-10a_mt8	0.96	-0.64	0.09	-0.90	0.07
12.9	36-10a_mt9	0.96	-0.65	0.13	-1.04	0.08
14.3	36-10a_mt10	0.96	-0.54	0.09	-0.92	0.06
15.7	36-10b_mt1	1.01	-0.78	0.10	-0.99	0.06
17.1	36-10b_mt2a	1.01	-0.42	0.10	-0.79	0.06
17.1	36-10b_mt2	0.99	-0.70	0.07	-1.04	0.07
18.6	36-10b_mt3a	1.03	-0.66	0.13	-0.80	0.10
20	36-10b_mt4	0.99	-0.44	0.13	-0.52	0.06
21.4	36-10b_mt5	1.01	-0.32	0.08	-0.48	0.06
21.4	36-10b_mt5	0.99	-0.76	0.12	-1.13	0.07
22.9	36-10b_mt6	1.00	-0.32	0.12	-0.61	0.10
24.3	36-10b_mt7	1.03	-0.45	0.12	-0.56	0.08
24.3	36-10b_mt7	0.97	-0.64	0.12	-1.05	0.06
25.7	36-10b_mt8	1.06	-0.35	0.10	-0.71	0.06
27.1	36-10b_mt9	1.05	-0.42	0.11	-0.58	0.07
28.6	36-10b_mt10	1.07	-0.36	0.10	-0.45	0.07
30	36-10b_mt11	1.04	-0.37	0.13	-0.65	0.08
30	36-10b_mt11	0.97	-0.56	0.10	-0.78	0.06
30	36-10_c_mt1	0.98	-0.57	0.07	-0.74	0.05
31.4	36-10_c_mt2	0.99	-0.55	0.11	-0.78	0.06
32.9	36-10_c_mt3a	0.98	-0.70	0.09	-0.98	0.09
34.3	36-10_c_mt4	0.99	-0.75	0.08	-0.96	0.05
35.7	36-10_c_mt5	0.93	-0.74	0.11	-0.95	0.06
37.1	36-10_c_mt6a	0.98	-0.71	0.07	-0.94	0.05
38.6	36-10_c_mt7	0.99	-0.74	0.07	-0.91	0.05
40	36-10_c_mt8	0.96	-0.52	0.09	-0.85	0.05
41.4	36-10_c_mt9	0.94	-0.57	0.08	-0.80	0.05
42.9	36-10_c_mt10	0.93	-0.44	0.09	-0.69	0.05
44.3	36-10_d_mt1	0.98	-0.69	0.10	-0.92	0.06
45.7	36-10_d_mt2	0.98	-0.74	0.10	-1.06	0.06
47.1	36-10_d_mt3	0.97	-0.72	0.08	-1.07	0.05
48.6	36-10_d_mt4	1.01	-0.78	0.07	-1.07	0.06
52.9	36-10_d_mt5	0.96	-0.58	0.11	-0.85	0.07

Position along drill core (mm)	Analysis number	Fe intensity relative to standard	δ^{56}Fe	2SE	δ^{57}Fe	2SE
54.3	36-10_d_mt6	0.96	-0.49	0.07	-0.77	0.07
55.7	36-10_d_mt7a	0.95	-0.46	0.11	-0.66	0.07
58.6	36-10_e_mt1	0.92	-0.69	0.11	-1.12	0.06
60	36-10_e_mt2	0.87	-0.71	0.19	-1.13	0.09
60	36-10_e_mt2	0.91	-0.74	0.12	-1.15	0.06
61.4	36-10_e_mt3	0.94	-0.71	0.10	-1.21	0.05
62.9	36-10_e_mt4	0.95	-0.61	0.09	-0.97	0.05
64.3	36-10_e_mt5	0.95	-0.59	0.09	-0.98	0.08
65	36-10_e_mt6	0.96	-0.64	0.11	-0.97	0.06
67.9	36-10_e_mt7	1.03	-0.60	0.11	-0.86	0.07
68.6	36-10_e_mt8	1.00	-0.68	0.10	-0.86	0.07
70	36-10_e_mt9a	1.00	-0.63	0.12	-0.85	0.06
71.4	36-10_e_mt10	1.01	-0.51	0.09	-0.58	0.08
Hematite						
65.7	36-10e_Hem1	0.97	-0.91	0.18	-1.29	0.10
66	36-10e_Hem2	0.97	-0.57	0.16	-0.97	0.09
65.4	36-10e_Hem6	0.96	-0.70	0.19	-1.02	0.10
66.3	36-10e_Hem3	1.06	-0.48	0.13	-0.64	0.08
65.4	36-10e_Hem6	1.01	-0.44	0.10	-0.67	0.08
65.7	36-10e_Hem7	1.01	-0.50	0.07	-0.73	0.05
8.3	36-10b_Hem1	0.98	-0.47	0.22	-0.50	0.10
8.9	36-10b_Hem3	0.98	-0.41	0.22	-0.59	0.10
5	36-10b_Hem4	0.94	-0.46	0.25	-0.62	0.12
50	36-10D_Hem_b1	1.00	-0.29	0.06	-0.34	0.05
50.7	36-10D_Hem_b2	1.02	-0.24	0.08	-0.23	0.06
51.4	36-10D_Hem_b3	1.02	-0.15	0.09	-0.15	0.05
52.1	36-10D_Hem_b4	1.01	-0.23	0.08	-0.44	0.06

3.3 *In situ* REE data

Given the distinct generations of magnetite in the Dales Gorge member BIF, which include "near-primary" magnetite that is characterized by low Si contents and low $\delta^{18}O_{SMOW}$ values, as well as hydrothermal/ metamorphic magnetite that has high Si contents and elevated $\delta^{18}O_{SMOW}$ values (5, 10), it was important to establish which generation of magnetite contained the major inventory of REEs, to determine whether the bulk sample Nd isotope compositions reflect low-temperature primary precipitates or introduction of Nd by later hydrothermal alteration and metamorphism. Based on BSE images, *in situ* determinations of Pr, Nd, and Sm concentrations were made next to pits from previous *in situ* O and Fe isotope analysis in Li et al. (5). Pr and Sm concentrations were determined based on ^{141}Pr and ^{147}Sm counts, respectively, and Nd concentrations were determined by combining ^{143}Nd, ^{145}Nd, and ^{146}Nd counts. Sample number or analysis ID are the same as those reported in Li et al. (5).

Table S3. Concentrations of Pr, Nd, and Sm in iron oxides in BIF samples based on i*n situ* laser ablation analysis and the corresponding O and Fe isotope composition of the same mineral domain.

	Pr (ppm)	Nd (ppm)	Sm (ppm)	δ^{18}O (‰)	δ^{56}Fe (‰)
16-7_443(euhedral)	0.06	0.34	0.07	4.65	
16-7_445(hem)	0.18	0.82	0.19	-4.27	0.54
16-7_446(hem)	0.17	0.90	0.18	-3.97	0.62
16-7_447(hem)	0.16	0.70	0.16	-3.89	0.60
20-4_456(euhedral)	0.01	0.06	0.02	3.97	1.02
20-4_457(euhedral)	0.00	0.01	0.00	3.08	1.12

	Pr (ppm)	Nd (ppm)	Sm (ppm)	$\delta^{18}O$ (‰)	$\delta^{56}Fe$ (‰)
20-4_460(hem)	0.26	1.23	0.29	-4.08	1.53
20-4_461(hem)	0.23	1.04	0.23	-3.18	1.31
22-3_471(lowSi)	0.04	0.18	0.05	1.93	0.12
22-3_476(highSi)	0.01	0.07	0.02	2.11	
22-3_476(lowSi)	0.04	0.17	0.04	-4.43	-0.09
22-3_476(lowSi)repeat	0.05	0.23	0.06	-4.43	-0.09
22-3_490(highSi)	0.01	0.03	0.01		
22-3_490(lowSi)	0.04	0.15	0.03	-3.60	-0.15
23-6_463(euhedral)repeat	0.01	0.05	0.01	4.39	0.43
23-6_464(euhedral)	0.23	1.23	0.29	2.88	0.19
23-6_464(euhedral)repeat	0.03	0.13	0.03	2.88	0.19
24-8_424(high-Si)	0.04	0.20	0.05		
24-8_424(low-Si)	0.17	0.75	0.14	-4.00	0.11
24-8_426(high-Si)	0.02	0.08	0.02	3.46	
24-8_426(low-Si)	0.18	0.75	0.17	-3.30	0.18
24-8_429(high-Si)	0.08	0.36	0.09		
24-8_429(low-Si)	0.23	0.95	0.18	-2.51	0.09
27-11_409(high-Si)	0.09	0.41	0.13	4.37	0.44
27-11_412(low-Si)	0.53	2.23	0.44	-1.76	0.24
27-11_415(high-Si)	0.05	0.24	0.08	4.59	0.24
27-11_additional1(high-Si)	0.06	0.32	0.15		
27-11_additional1(low-Si)	0.21	0.89	0.19		
27-11_additional2(high-Si)	0.02	0.10	0.04		
27-11_additional2(low-Si)	0.26	1.20	0.26		
30-9B_505(high-Si)	0.11	0.52	0.23		
30-9B_505(low-Si)	0.13	0.56	0.25	0.72	0.16
32-3_398(hem)	0.02	0.10	0.02	-4.44	-0.34
32-3_400(euhedral)	0.07	0.26	0.05	5.05	-0.42
32-3_401(euhedral)	0.01	0.02	0.01	5.18	-0.47
32-3_401(hem)	0.08	0.31	0.07		
34-1_381(euhedral)	0.01	0.05	0.02	4.44	-0.12
34-1_383(hem)	0.19	1.35	0.35	-4.92	0.13
34-1_384(hem)	0.10	0.66	0.18	-5.62	0.34
34-1_additional1(hem)	0.05	0.36	0.11		
36-10_396(euhedral)	0.00	0.02	0.00	2.95	-0.62
36-10_396(euhedral)	0.01	0.04	0.01	2.95	-0.62
36-10_397(euhedral)	0.00	0.02	0.00	3.43	-0.65
36-10_additional1(hem)	0.02	0.13	0.02		
9-12_448(highSi)	0.00	0.01	0.00	3.63	0.20
9-12_449(lowSi)	0.15	0.76	0.21	-0.66	0.22
9-12_450(highSi)	0.01	0.05	0.02		
9-12_450(lowSi)	0.12	0.65	0.17	3.11	0.07
9-12_450(lowSi)repeat	0.23	1.14	0.28	3.11	0.07
9-12_451(highSi)	0.02	0.09	0.02	3.68	0.18
9-12_451(lowSi)	0.29	1.45	0.38		
16-7_443(euhedral)	0.06	0.34	0.07	4.65	
16-7_445(hem)	0.18	0.82	0.19	-4.27	0.54
16-7_446(hem)	0.17	0.90	0.18	-3.97	0.62
16-7_447(hem)	0.16	0.70	0.16	-3.89	0.60

	Pr (ppm)	**Nd (ppm)**	**Sm (ppm)**	**δ^{18}O (‰)**	**δ^{56}Fe (‰)**
20-4_456(euhedral)	0.01	0.06	0.02	3.97	1.02
20-4_457(euhedral)	0.00	0.01	0.00	3.08	1.12
20-4_460(hem)	0.26	1.23	0.29	-4.08	1.53
20-4_461(hem)	0.23	1.04	0.23	-3.18	1.31
22-3_471(lowSi)	0.04	0.18	0.05	1.93	0.12
22-3_476(highSi)	0.01	0.07	0.02	2.11	
22-3_476(lowSi)	0.04	0.17	0.04	-4.43	-0.09
22-3_476(lowSi)repeat	0.05	0.23	0.06	-4.43	-0.09
22-3_490(highSi)	0.01	0.03	0.01		
22-3_490(lowSi)	0.04	0.15	0.03	-3.60	-0.15
23-6_463(euhedral)repeat	0.01	0.05	0.01	4.39	0.43
23-6_464(euhedral)	0.23	1.23	0.29	2.88	0.19
23-6_464(euhedral)repeat	0.03	0.13	0.03	2.88	0.19
24-8_424(high-Si)	0.04	0.20	0.05		
24-8_424(low-Si)	0.17	0.75	0.14	-4.00	0.11
24-8_426(high-Si)	0.02	0.08	0.02	3.46	
24-8_426(low-Si)	0.18	0.75	0.17	-3.30	0.18
24-8_429(high-Si)	0.08	0.36	0.09		
24-8_429(low-Si)	0.23	0.95	0.18	-2.51	0.09
27-11_409(high-Si)	0.09	0.41	0.13	4.37	0.44
27-11_412(low-Si)	0.53	2.23	0.44	-1.76	0.24
27-11_415(high-Si)	0.05	0.24	0.08	4.59	0.24
27-11_additional1(high-Si)	0.06	0.32	0.15		
27-11_additional1(low-Si)	0.21	0.89	0.19		
27-11_additional2(high-Si)	0.02	0.10	0.04		
27-11_additional2(low-Si)	0.26	1.20	0.26		
30-9B_505(high-Si)	0.11	0.52	0.23		
30-9B_505(low-Si)	0.13	0.56	0.25	0.72	0.16
32-3_398(hem)	0.02	0.10	0.02	-4.44	-0.34
32-3_400(euhedral)	0.07	0.26	0.05	5.05	-0.42
32-3_401(euhedral)	0.01	0.02	0.01	5.18	-0.47
32-3_401(hem)	0.08	0.31	0.07		
34-1_381(euhedral)	0.01	0.05	0.02	4.44	-0.12
34-1_383(hem)	0.19	1.35	0.35	-4.92	0.13
34-1_384(hem)	0.10	0.66	0.18	-5.62	0.34
34-1_additional1(hem)	0.05	0.36	0.11		
36-10_396(euhedral)	0.00	0.02	0.00	2.95	-0.62
36-10_396(euhedral)	0.01	0.04	0.01	2.95	-0.62
36-10_397(euhedral)	0.00	0.02	0.00	3.43	-0.65
36-10_additional1(hem)	0.02	0.13	0.02		
9-12_448(highSi)	0.00	0.01	0.00	3.63	0.20
9-12_449(lowSi)	0.15	0.76	0.21	-0.66	0.22
9-12_450(highSi)	0.01	0.05	0.02		
9-12_450(lowSi)	0.12	0.65	0.17	3.11	0.07
9-12_450(lowSi)repeat	0.23	1.14	0.28	3.11	0.07
9-12_451(highSi)	0.02	0.09	0.02	3.68	0.18
9-12_451(lowSi)	0.29	1.45	0.38		

4. Additional discussion

4.1 Potential influence of metamorphism on REE and Nd isotope compositions

The Sm-Nd isotopic data measured from in this study form a linear array on a ^{143}Nd/^{144}Nd-^{147}Sm/^{144}Nd plot, with a slope corresponding to an age of 2074±150 Ma (calculated using IsoPlot® (18)), far younger than the accepted 2.5 Ga deposition age for the Dales Gorge Member (Figure S5-A). This is consistent with the previous Sm-Nd isotope studies of Alibert and McCulloch (19), who obtained a ^{143}Nd/^{144}Nd-^{147}Sm/^{144}Nd isochron age of 2140±30 Ma for samples of Dales Gorge and Joffre member of the Brockman Iron Formation. Alibert and McCulloch (19) suggested that the apparently young ^{147}Sm/^{144}Nd-^{143}Nd/^{144}Nd age reflects a metamorphic event at ~2.1 Ga that reset Sm-Nd isotope systems. However, such Sm-Nd isotopic data array with slightly less steep slope could be alternatively explained by mixing between two end members at 2.5 Ga, one that had mantle ^{143}Nd/^{144}Nd signature at and low (~0.08) ^{147}Sm/^{144}Nd ratio, and one that had crustal ^{143}Nd/^{144}Nd signature at and high (>0.18) ^{147}Sm/^{144}Nd ratio (Figure S5-A). If the Sm-Nd isotope systematics are assumed to have remained undisturbed since BIF deposition at 2.5 Ga, the ^{147}Sm/^{144}Nd-^{143}Nd/^{144}Nd "age" inferred by Alibert and McCulloch (19) is equivalent to an array at 2.5 Ga that would produce a negative correlation between ε_{Nd} (calculated at 2.5Ga) and Sm/Nd ratio (Figure S5-B).

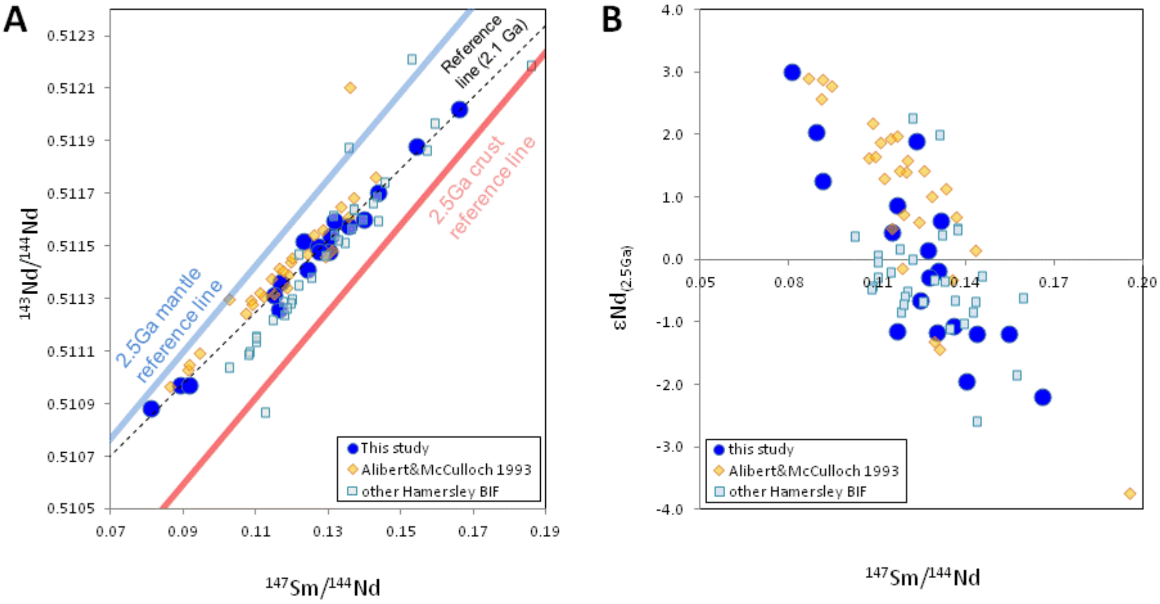

Figure S5. A. ^{147}Sm/^{144}Nd-^{143}Nd/^{144}Nd plot for samples from Hamersley Group, data measured from this study plot a long a reference isochron of 2074±150 Ma, consistent with those of Alibert and McCulloch (19), for comparison, 2.5 Ga reference isochrons for mantle and crustal samples are also plotted. **B.** Plot of ε_{Nd} (calculated at 2.5Ga) versus ^{147}Sm/^{144}Nd for samples from the Hamersley Group. Data are compiled from this study and Alibert and McCulloch (19).

Alibert and McCulloch (19) discounted two end-member mixing as the mechanism to explain the correlations as shown in Figure S5-B, arguing that mixing between a hydrothermal source that has a positive ε_{Nd} value and high Sm/Nd ratio, and a continental source that has a negative ε_{Nd} value and low

Sm/Nd ratio would produce a positive trend of ε_{Nd} vs Sm/Nd, which is not observed. Note that by the time of Alibert and McCulloch (19), processes to fractionate Sm/Nd ratios in seawater had not been well documented, so they did not consider the effects of progressive oxidation of Fe from a hydrothermal plume, and its effects on Sm/Nd rations, nor the possibility that a continental shelf source (pore fluids) would have fractionated Sm/Nd ratios relative to bulk continental detritus.

Here, we address the issue of metamorphism as it bears on Nd isotopes and REEs in Hamersley Group. First, we note that REEs are generally considered relatively immobile elements that are resistant to metamorphism (20). The peak metamorphic temperature recorded in the Hamersley Group samples did not exceed 350 °C (5, 7, 21), and so cannot be considered to be high grade. Second, it is difficult to envision a process at 2.1 Ga that homogenized ^{143}Nd/^{144}Nd ratios in BIF and shale samples at a basin-wide scale, but did not homogenize REE patterns, including ^{147}Sm/^{144}Nd ratios. Furthermore, although the Dales Gorge member BIF samples plot along a 2.1 Ga ^{143}Nd/^{144}Nd-^{147}Sm/^{144}Nd isochron in the study by Alibert and McCulloch (19), samples of the slightly older Marra Mamba BIF of the Hamersley Group plot along a ^{143}Nd/^{144}Nd-^{147}Sm/^{144}Nd reference isochron that corresponds to an age of 2.6 Ga, which is consistent with the depositional age; a later metamorphic event should have affected both the Dales Gorge and the Marra Mamba BIFs. Third, *in situ* O isotope analyses show that a substantial portion of iron oxides (hematite and low-Si magnetite) in the Hamersley BIF have low $\delta^{18}O_{SMOW}$ values, indicating insignificant or negligible resetting of O isotope compositions by hydrothermal or metamorphic events (5). In particular, *in situ* REE analyses (Figure S6) show that the low-$\delta^{18}O_{SMOW}$ iron oxide minerals (hematite and low-Si magnetite), which are the most primary iron oxides, contain the highest REE contents, significantly higher than the high-$\delta^{18}O_{SMOW}$ iron oxide minerals (silician magnetite and euhedral magnetite) that are characteristic of hydrothermal/ metamorphic oxides. These observations indicate that 1) the REEs in bulk samples of the BIFs minerals record "near-primary" signatures for iron oxide precipitation, and 2) the REEs in the BIFs were not reset by metamorphic or hydrothermal events. Based on the above discussions, the 2.1 Ga metamorphic event proposed by Alibert and McCulloch (19) is incorrect, and instead is an artifact of the correlation between initial ^{143}Nd/^{144}Nd ratios calculated at 2.5 Ga and Sm/Nd ratios.

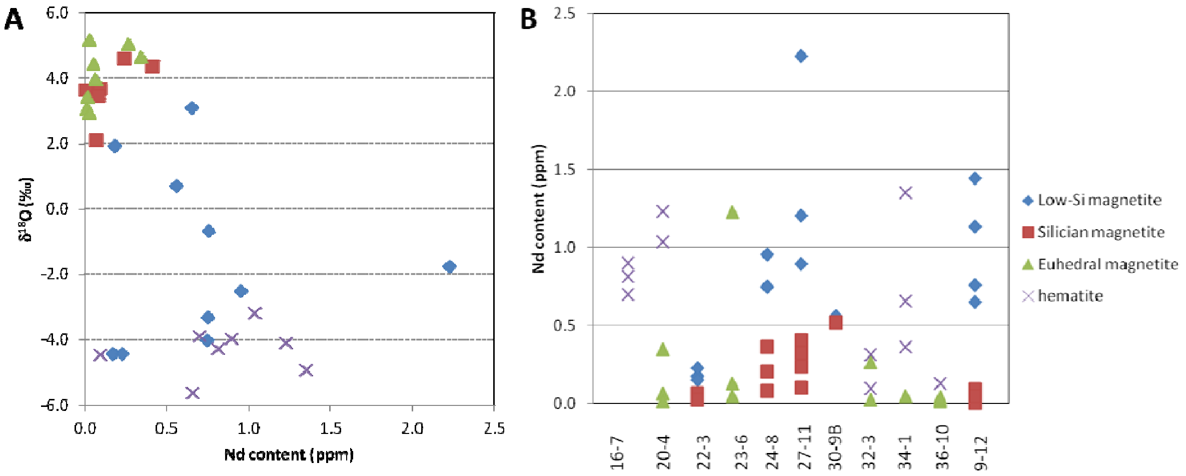

Figure S6. A. Plot of Nd contents and $\delta^{18}O_{SMOW}$ value in iron oxides from Dales Gorge member BIF. B. Nd contents in iron oxides in different BIF samples.

4.2 Rayleigh model for Nd-Fe isotope variations and model sensitivity

4.2.1 Details of the model

The correlation between δ^{56}Fe and ε_{Nd} values from the Dales Gorge member BIF samples provides an opportunity to test the currently accepted model that the source of Fe for BIFs is entirely hydrothermal. According to this hypothesis, BIFs that have negative δ^{56}Fe values would reflect a Rayleigh process, where partial oxidation of hydrothermal $Fe(II)_{aq}$, followed by precipitation as high-δ^{56}Fe ferric Fe hydroxides from the hydrothermal plume, produce low-δ^{56}Fe values in the remaining fluid that eventually leads to formation of low-δ^{56}Fe precipitates (22-24). This model can be tested using Nd isotopes because hydrothermal and continental sources of Nd have distinct isotopic compositions (25), and the high partitioning of the REEs to Fe hydroxides makes a progressive hydrothermal precipitation process sensitive to identification of a non-hydrothermal component.

Because a large variation in ε_{Nd} values (calculated at 2.5 Ga) has been found in the Dales Gorge member BIF samples (-2.2 to +3.0), we assume a two end-member scenario for Nd, where the initial hydrothermal fluid had an ε_{Nd} value of +3.0, and the ambient “Archean seawater” had an ε_{Nd} value of -3.0. These are appropriate values for the mantle and average continental crust at 2.5 Ga (25). The hydrothermal end member fluid is assumed to have had an Fe content of 100 µmol/L and a δ^{56}Fe value of 0‰, following the discussion in Czaja et al. (26). The Nd content of the hydrothermal end member fluid was set as 0.028 ppb, assuming a $Nd/Fe=5*10^{-6}$, based on the study of Olivarez and Owen (27) on REE/Fe ratios in modern hydrothermal vent fluids. For the other end member, “Archean seawater”, Fe content was set to zero to provide the most sensitive test possible of a Rayleigh fractionation model in producing BIFs that have negative δ^{56}Fe values. It is also conceptually consistent with a model that assumes a shallow, low-$Fe(II)_{aq}$ zone where oxidation of Fe occurs. If non-zero initial Fe contents are assumed for the "Archean seawater" component, the decrease in δ^{56}Fe values, relative to percent oxidation, will be muted, and hence it will be more difficult for the model to produce low δ^{56}Fe values. The "Archean seawater" component for Nd content was set at 0.000115 ppb, based on the study of Sholkovitz (28) on modern estuary water with seawater salinity.

We use a constant Fe isotope fractionation factor between $Fe(OH)_3$ and Fe^{2+} solution, where $\Delta^{56}Fe_{Fe(OH)3-Fe2+}$ was set as +1.5‰, based on the studies of abiologic and biologic $Fe(II)_{aq}$ oxidation (29-30). It is possible that the $\Delta^{56}Fe_{Fe(OH)3-Fe2+}$ fractionation factor could be as high as +4‰ (31), and such a choice would provide even poorer fits to the data. During $Fe(OH)_3$ precipitation, Nd in both hydrothermal fluid and ambient “Archean seawater” was scavenged by adsorption onto the $Fe(OH)_3$ surface. The K_d is defined as $(Nd/Fe)_{Fe(OH)3}/(Nd/Fe)_{solution}$. The Nd isotope composition of the $Fe(OH)_3$ precipitate was calculated by mixing between the hydrothermal Nd component (which decreased with progression of $Fe(II)_{aq}$ oxidation due to adsorption onto $Fe(OH)_3$), and a constant ambient “Archean seawater” background Nd. This assumption is reasonable as dust/particle dissolution is the main provider of terrestrial REEs in the modern open ocean (32; and references therein).

We applied a numerical modeling approach, combining a Rayleigh distillation process of hydrothermal $Fe(II)_{aq}$ oxidation, divided into 100 steps, with mixing with "Archean seawater" at each step. In each step, 1 percent of $Fe(II)_{aq}$ was oxidized to $Fe(OH)_3$ at a constant $\Delta^{56}Fe_{Fe(OH)3-Fe2+}$ fractionation factor, as well as a fixed K_d factor for Nd adsorption. After each step, the content and isotopic composition of Fe and Nd in solution was recalculated and used for the next step of $Fe(II)_{aq}$ oxidation and precipitation. Conceptually, the hydrothermal fluid is envisioned as laterally spreading out from a hydrothermal plume source, as has been suggested by many workers (22-24). Therefore, the Nd and Fe isotope composition of the $Fe(OH)_3$ precipitates in each step are considered as individual "packets" that eventually find their way to the site of BIF deposition. The model is shown schematically in Figure S7, and the original code/file for modeling is in the *Excel* Appendix.

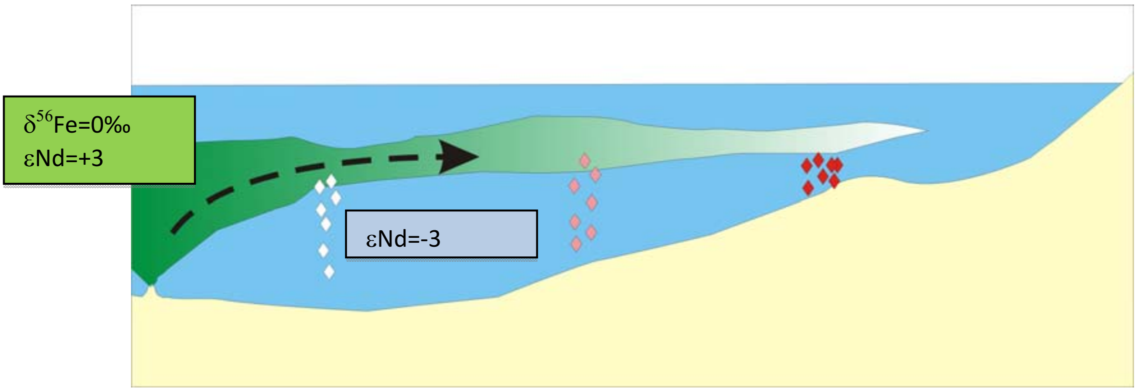

Figure S7. Cartoon showing the Rayleigh distillation model for oxidation and precipitation of hydrothermally sourced $Fe(II)_{aq}$. Different extents of oxidation and precipitation of iron hydroxides is illustrated by the distinct colors, as a function of distance from the plume origin.

4.2.2 Test of the sensitivity of the model

Sensitivity tests have been done to assess the influence of different parameters of the model on the Nd-Fe isotope compositions produced for $Fe(OH)_3$ precipitates. The results of sensitivity tests that varied REE K_d (Figure S8), $\Delta^{56}Fe_{Fe(OH)3\text{-}Fe2+}$ fractionation factor (Figure S9), and Nd content of ambient “Archean seawater” (Figure S10) show that although these parameters all affect the Nd-Fe isotope variations, it is very difficult to reproduce the data, suggesting that mixing of water masses, as discussed in the main text, is the most likely explanation for the isotopic variations. A partial oxidation model can only be fit through the observed Nd-Fe isotope trend if the K_d for Nd was extremely low, restricted to between 7 and 4. In addition, the Nd concentration of ambient “Archean seawater” must be at modern seawater values, or one to two orders of magnitudes lower, in combination with a very low K_d. The K_d values for Nd measured from modern MOR vent fluid and sediments are on the order of 10^2 (27), and experimentally obtained K_d values for Nd on different type of Fe oxide or hydroxide vary from 10^3 to 10^6 (33-35). Although MOR vent fluids may have K_d’s as low as 12, this was found in only one sample, and K_d’s that are one to two orders of magnitude higher are more typical (27). It therefore seems unreasonable to call upon very low K_d values between 7 and 4. Although decreasing the Nd content of ambient “Archean seawater” by one or two orders of magnitude provides an improved fit between the Rayleigh model and the measured data, the higher heat flux of the Archean earth (e.g., 36 and references therein) should result in higher volcanism intensity, producing higher ash deposition in the Archean ocean, thus, we would argue, higher ambient “Archean seawater” Nd concentrations. Moreover, models that use very low “Archean seawater” Nd concentrations can only be fit to the data using a low K_d of ~7, which, as noted above, is unrealistically low. Finally, a range of $\Delta^{56}Fe_{Fe(OH)3\text{-}Fe2+}$ fractionation factors are possible, dependent on extent of equilibrium versus kinetic exchange. As discussed by (31), Fe-Si co-precipitates are the most likely primary Fe(III) hydroxide in the Archean oceans, and $\Delta^{56}Fe_{Fe(OH)3\text{-}Fe2+}$ fractionation factors for such materials can approach +4‰; use of fractionation factors higher than the conservative +1.5‰ produce very poor fits to the data. Use of a smaller $\Delta^{56}Fe_{Fe(OH)3\text{-}Fe2+}$ fractionation factor such as +0.5‰ provides a better fit to some of the data, although it cannot produce the very negative $\delta^{56}Fe$ values.

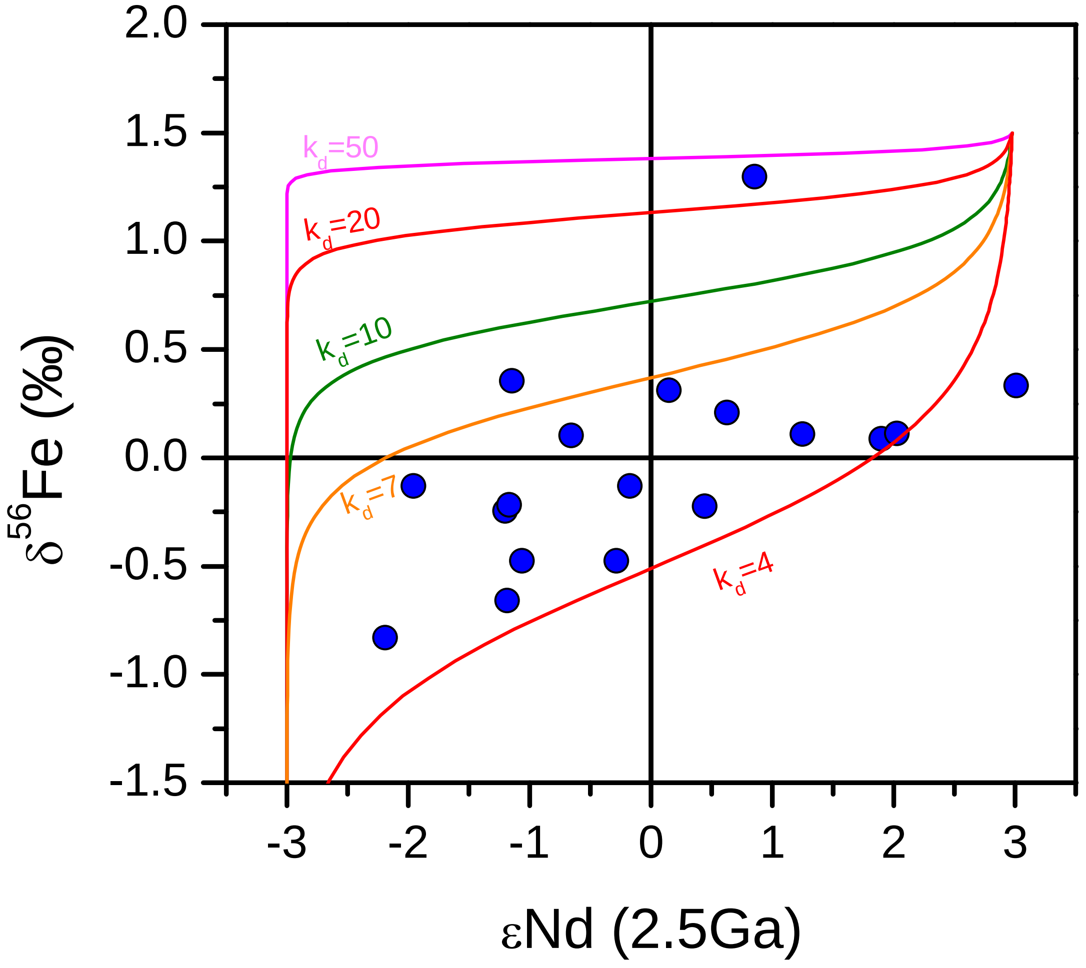

Figure S8. Sensitivity test of Rayleigh model for oxidation of hydrothermal fluid that contains 5600 ppb $Fe(II)_{aq}$ (δ^{56}Fe =0‰), and 0.028 ppb of Nd (ε_{Nd}=+3) in an Archean ocean that contains 0.000115 ppb Nd (ε_{Nd} =-3). The Fe isotope fractionation factor ($\Delta^{56}Fe_{Fe(OH)3-Fe2+}$) is set at a constant value of +1.5 ‰. The partition coefficient for Nd between $Fe(OH)_3$ and aqueous solution is set at different values (50, 20, 10, 7, 4) to compare the modeled δ^{56}Fe-ε_{Nd} data of $Fe(OH)_3$ precipitates and measured BIF isotope data.

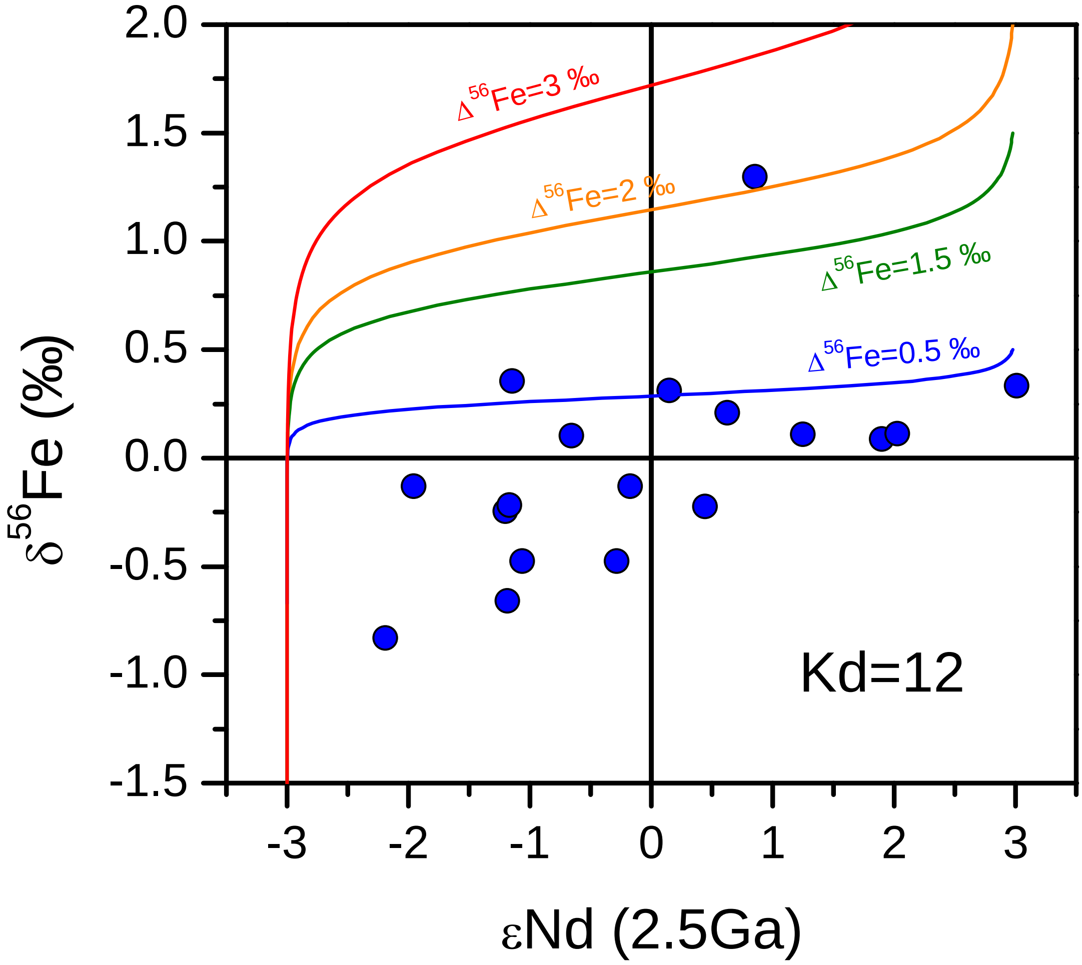

Figure S9. Sensitivity test of Rayleigh model for oxidation of hydrothermal fluid that contains 5600 ppb Fe(II)aq (δ^{56}Fe =0‰), and 0.028 ppb of Nd (ε_{Nd}=+3) in an Archean ocean that contains 0.000115 ppb Nd (ε_{Nd} =-3). The K_d value Nd is set at a constant value of 12, the minimum possible value based on field studies. Iron isotope fractionation factor ($\Delta^{56}Fe_{Fe(OH)3-Fe2+}$) is set at different values (0.5‰, 1.5‰, 2‰, 3‰) to compare the modeled δ^{56}Fe-ε_{Nd} data of $Fe(OH)_3$ precipitates and measured BIF isotope data.

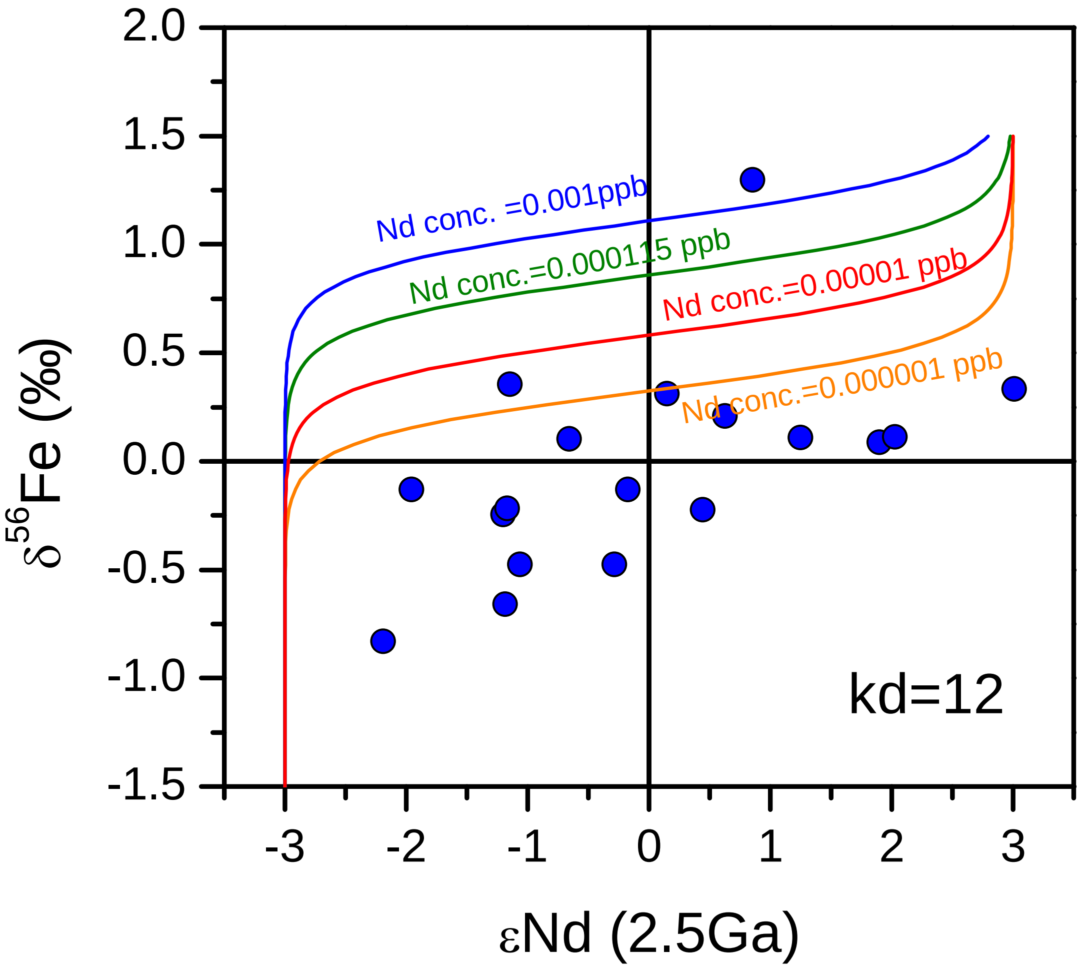

Figure S10. Sensitivity test of Rayleigh model for oxidation of hydrothermal fluid that contains 5600 ppb $Fe(II)_{aq}$ ($\delta^{56}Fe$ =0‰), and 0.028 ppb of Nd (ε_{Nd} =+3) in an Archean ocean that contains variable concentration of Nd (ε_{Nd} =-3). The K_d value Nd is set at a constant value of 12, the minimum possible value based on field studies. Iron isotope fractionation factor ($\Delta^{56}Fe_{Fe(OH)3\text{-}Fe2+}$) is set at a constant value of +1.5 ‰. The Archean ocean Nd concentration is set at different values (0.001 ppb, 0.000115 ppb, 0.00001 ppb, and 0.000001 ppb) to compare the modeled $\delta^{56}Fe$- ε_{Nd} data of $Fe(OH)_3$ precipitates and measured BIF isotope data.

5. References

1. Trendall AF & Blockley JG (1970) *The Iron-Formations of the Precambrian Hamersley Group, Western Australia* (Geological Survey Western Australia Bulletin 119) p 366.

2. Trendall AF, Compston W, Nelson DR, De Laeter JR, & Bennett VC (2004) SHRIMP zircon ages constraining the depositional chronology of the Hamersley Group, Western Australia. *Australian Journal of Earth Sciences* 51(5):621-644.
3. Trendall AF & Blockley JG (1968) Stratigraphy of the Dales Gorge Member of the Brockman Iron formation in the Precambrian Hamersley Group of Western Australia. in *Geological Survey of Western Australia Annual Report for 1967*, pp 48-53.
4. Ewers WE & Morris RC (1981) Studies of the Dales Gorge Member of the Brockman Iron Formation, Western Australia. *Economic Geology* 76(7):1929-1953.
5. Li W*, et al.* (2013) Contrasting behavior of oxygen and iron isotopes in banded iron formations revealed by in situ isotopic analysis. *Earth and Planetary Science Letters* 384(0):132-143.
6. Johnson CM, Beard BL, Klein C, Beukes NJ, & Roden EE (2008) Iron isotopes constrain biologic and abiologic processes in banded iron formation genesis. *Geochimica et Cosmochimica Acta* 72(1):151-169.
7. Becker RH & Clayton RN (1976) Oxygen isotope study of a Precambrian banded iron-formation, Hamersley Range, Western Australia. *Geochimica et Cosmochimica Acta* 40(10):1153-1165.
8. Becker RH & Clayton RN (1972) Carbon isotopic evidence for the origin of a banded iron-formation in Western Australia. *Geochimica et Cosmochimica Acta* 36(5):577-595.
9. Heck PR*, et al.* (2011) SIMS analyses of silicon and oxygen isotope ratios for quartz from Archean and Paleoproterozoic banded iron formations. *Geochimica et Cosmochimica Acta* 75(20):5879-5891.
10. Huberty JM*, et al.* (2012) Silician magnetite from the Dales Gorge Member of the Brockman Iron Formation, Hamersley Group, Western Australia. *American Mineralogist* 97:26-37.
11. Beard BL*, et al.* (2003) Application of Fe isotopes to tracing the geochemical and biological cycling of Fe. *Chemical Geology* 195(1-4):87-117.
12. Beard BL*, et al.* (2010) Iron isotope fractionation between aqueous ferrous iron and goethite. *Earth and Planetary Science Letters* 295(1-2):241-250.
13. Stookey LL (1970) Ferrozine---a new spectrophotometric reagent for iron. *Analytical Chemistry* 42(7):779-781.
14. d'Abzac F-X, Czaja AD, Beard BL, Schauer JJ, & Johnson CM (2014) Iron Distribution in Size-Resolved Aerosols Generated by UV-Femtosecond Laser Ablation: Influence of Cell Geometry and Implications for In Situ Isotopic Determination by LA-MC-ICP-MS. *Geostandards and Geoanalytical Research* 38(3):293-309.
15. Morris RC (1993) Genetic modelling for banded iron-formation of the Hamersley Group, Pilbara Craton, Western Australia. *Precambrian Research* 60(1–4):243-286.
16. Drever JI (1974) Geochemical Model for the Origin of Precambrian Banded Iron Formations. *Geological Society of America Bulletin* 85(7):1099-1106.
17. Li Y-L (2014) Micro- and nanobands in late Archean and Palaeoproterozoic banded-iron formations as possible mineral records of annual and diurnal depositions. *Earth and Planetary Science Letters* 391(0):160-170.
18. Ludwig KR (1999) Using Isoplot/Ex, Version 2.01: a geochronological toolkit for Microsoft Excel. *Berkeley Geochronology Center Special Publication* 1a:1-47.
19. Alibert C & McCulloch MT (1993) Rare earth element and neodymium isotopic compositions of the banded iron-formations and associated shales from Hamersley, western Australia. *Geochimica et Cosmochimica Acta* 57(1):187-204.
20. Faure G (1986) *Principles of isotope geology* (John Wiley & Sons, New York) p 589.
21. Rasmussen B, Fletcher IR, & Sheppard S (2005) Isotopic dating of the migration of a low-grade metamorphic front during orogenesis. *Geology* 33(10):773-776.

22. Planavsky N*, et al.* (2012) Iron isotope composition of some Archean and Proterozoic iron formations. *Geochimica et Cosmochimica Acta* 80:158-169.
23. Rouxel lJ, Bekker n, & Edwards aJ (2005) Iron isotope constraints on the Archean and Paleoproterozoic ocean redox state. *Science* 307:1088-1091.
24. Bekker A*, et al.* (2010) Iron Formation: The Sedimentary Product of a Complex Interplay among Mantle, Tectonic, Oceanic, and Biospheric Processes. *Economic Geology* 105(3):467-508.
25. DePaolo DJ (1988) *Neodymium Isotope Geochemistry: An Introduction* (Springer-Verlag, Heidelberg) p 187.
26. Czaja AD*, et al.* (2012) Evidence for free oxygen in the Neoarchean ocean based on coupled iron-molybdenum isotope fractionation. *Geochimica et Cosmochimica Acta* 86:118-137.
27. Olivarez AM & Owen RM (1989) REE/Fe variations in hydrothermal sediments: Implications for the REE content of seawater. *Geochimica et Cosmochimica Acta* 53(3):757-762.
28. Sholkovitz ER (1993) The geochemistry of rare earth elements in the Amazon River estuary. *Geochimica et Cosmochimica Acta* 57(10):2181-2190.
29. Bullen TD, White AF, Childs CW, Vivit DV, & Schulz MS (2001) Demonstration of significant abiotic iron isotope fractionation in nature. *Geology* 29(8):699-702.
30. Croal LR, Johnson CM, Beard BL, & Newman DK (2004) Iron isotope fractionation by Fe(II)-oxidizing photoautotrophic bacteria. *Geochimica et Cosmochimica Acta* 68(6):1227-1242.
31. Wu L, Percak-Dennett EM, Beard BL, Roden EE, & Johnson CM (2012) Stable iron isotope fractionation between aqueous Fe(II) and model Archean ocean Fe-Si coprecipitates and implications for iron isotope variations in the ancient rock record. *Geochimica et Cosmochimica Acta* 84:14-28.
32. Ling H-F*, et al.* (2005) Differing controls over the Cenozoic Pb and Nd isotope evolution of deepwater in the central North Pacific Ocean. *Earth and Planetary Science Letters* 232(3–4):345-361.
33. Koeppenkastrop D & De Carlo EH (1992) Sorption of rare-earth elements from seawater onto synthetic mineral particles: An experimental approach. *Chemical Geology* 95(3–4):251-263.
34. Quinn KA, Byrne RH, & Schijf J (2006) Sorption of yttrium and rare earth elements by amorphous ferric hydroxide: Influence of pH and ionic strength. *Marine Chemistry* 99(1–4):128-150.
35. Schijf J & Marshall KS (2011) YREE sorption on hydrous ferric oxide in 0.5 M NaCl solutions: A model extension. *Marine Chemistry* 123(1–4):32-43.
36. Holland HD (2009) Why the atmosphere became oxygenated: A proposal. *Geochimica et Cosmochimica Acta* 73(18):5241-5255.